JOURNAL OF SOLID STATE CHEMISTRY 113, 303–311 (1994)

Resistivity and Magnetism of AMn_2P_2 (A = Sr, Ba): The Effect of Structure Type on Physical Properties

Stephanie L. Brock,* J. E. Greedan,† and Susan M. Kauzlarich*,[1]

*Department of Chemistry, University of California, Davis, California 95616; and †Institute for Materials Research, McMaster University, Hamilton, Ontario, Canada, L8S4M1

Received October 20, 1993; accepted March 16, 1994

AMn_2P_2(A = Sr, Ba) is an example of a composition that can assume a different structure type depending on the identity of the cation. $BaMn_2P_2$ crystallizes in the $ThCr_2Si_2$ structure type ($I4/mmm$), and $SrMn_2P_2$ crystallizes in the $CaAl_2Si_2$ structure type ($P\bar{3}m1$). Temperature-dependent magnetic susceptibility, neutron diffraction, and resistivity measurements were obtained for the two compounds. Neutron diffraction shows that $BaMn_2P_2$ exhibits long-range antiferromagnetic ordering at room temperature. Mn(II) is high spin, with ordered moment 4.2 (1) μ_B, and the magnetic structure is type G. Magnetic susceptibility measurements show no maxima up to 750 K, indicating that the transition temperature, T_c, is very high. $SrMn_2P_2$ is antiferromagnetic below T_c = 53(1) K, as determined from the temperature dependence of the magnetic reflections. There are two distinct sets of magnetic reflections distinguished by different temperature dependencies and indexing schemes. The magnetic structure is evidently complex, but was not determined. Both compounds exhibit semiconducting resistivity behavior with E_a = 0.073(1) eV ($BaMn_2P_2$) and 0.0129(2) eV ($SrMn_2P_2$). The properties of $BaMn_2P_2$ and $SrMn_2P_2$ are discussed in light of their structures and previous theoretical investigations by Zheng and Hoffmann.

INTRODUCTION

In the series of compounds AMn_2P_2 (A = alkaline earth), there is a change in structure type observed when the lighter alkaline earth metals (Ca, Sr) are replaced by Ba. $BaMn_2P_2$ crystallizes in the $ThCr_2Si_2$ structure type, whereas AMn_2P_2 (A = Ca, Sr) crystallizes in the $CaAl_2Si_2$ structure type (Fig. 1). The presence of the same chemical unit, $Mn_2P_2^{-2}$, in these compounds allows for a correlation of the properties to the different structures.

Investigations of $ThCr_2Si_2$-type compounds have been numerous as these materials exhibit a variety of interesting properties. Examples include $LaRu_2P_2$ (1), which is a superconductor, and heavy fermion systems such as $CeCu_2Si_2$ (2, 3) or URu_2Si_2 (3, 4). Extensive magnetic studies have been performed on the compounds RM_2X_2 (R = rare earth metal, M = transition metal, and X = Si, Ge) (5). Of the compounds studied, only in those with Mn has an ordering of the transition metal lattice been observed. Many of the transition metal phosphides of the $ThCr_2Si_2$ type have also been studied. Among the first row transition metals the focus has been on compounds of Fe, Co, and Ni with alkaline earth, or more frequently, rare earth cations (6–11). No ordering of the transition metal lattice has been observed in these compounds for Fe or Ni; however, among the Co compounds, magnetism due to the transition metal lattice is sometimes observed (8, 10). No magnetic studies have been reported for Mn containing pnictides of the $ThCr_2Si_2$ type.

Magnetic studies of $CaAl_2Si_2$-type compounds have so far been limited to the study of rare earth cations with nonmagnetic $M_2Pn_2^{-2}$ (M = d^0, d^{10} metal; Pn = P, As, Sb, Bi) sublattices (6, 12). There have been no reports on the magnetic and electronic properties of the compounds AMn_2Pn_2 (A = Ca, Sr; Pn = P, As, Sb) other than a brief report on $SrMn_2As_2$, which indicated that the magnetism is Curie–Weiss, but cautioned that the data are unreliable (13).

Zheng and Hoffmann have performed theoretical studies on the stabilities of the two structure types for d^5 metals and have predicted their band structures (14). Based on their calculations, the compounds AMn_2P_2 (A = Sr, Ba) are expected to demonstrate significant differences in their physical properties. We were interested in studying these properties to see how well they relate to Zheng and Hoffmann's theories. Therefore, we have performed magnetic and electronic property measurements, and neutron diffraction studies on $BaMn_2P_2$ ($ThCr_2Si_2$-type) and $SrMn_2P_2$ ($CaAl_2Si_2$-type). This paper will describe these properties and discuss how they relate to the different structures and to Zheng and Hoffmann's theoretical calculations.

[1] To whom correspondence should be addressed.

0022-4596/94 $6.00

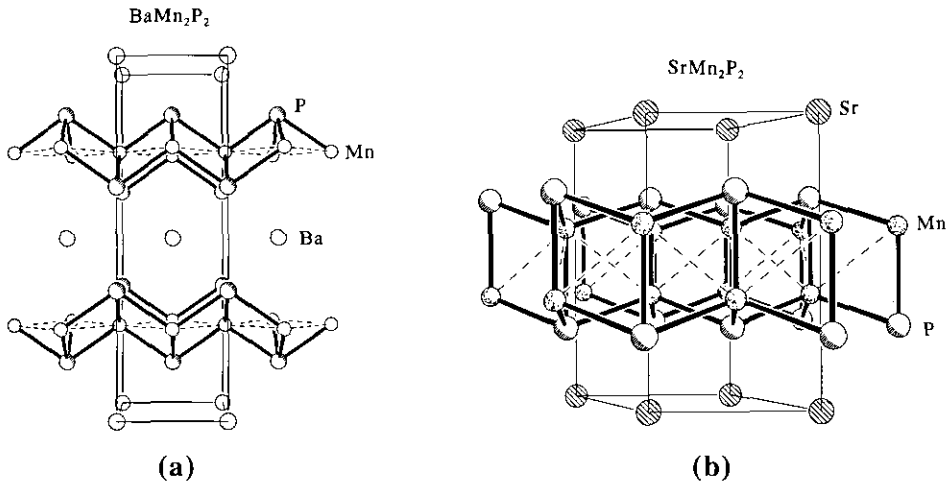

FIG. 1. The unit cells of (a) $BaMn_2P_2$ ($I4/mmm$, $ThCr_2Si_2$ type) and (b) $SrMn_2P_2$ ($P\bar{3}m1$, $CaAl_2Si_2$ type).

EXPERIMENTAL

Materials

Phosphorus (Johnson Matthey, 99.999%), barium (APL Engineering, 99.9%), and strontium (Strem, 99.95%) were used as received without further purification. Manganese flake (Johnson Matthey, 99.9%) was etched with 15% by volume HNO_3 in methanol and rinsed with acetone before use. All materials were handled in a dry box under argon. The Mn and P were ground with a mortar and pestle to produce powders, and the Ba or Sr was cut as finely as possible.

Synthesis

Stoichiometric mixtures of the elements were pressed into a pellet (2000–5000 psi), placed in an alumina boat, and sealed in a quartz ampoule under 0.5 atm of argon. The samples were then heated to 900°C by 30°C/hr and left for 20 hr. The tubes were cooled to room temperature at a rate of 100°C/hr. The pellets were ground up, pressed again, and heated once or twice more to 1100°C (100°C/hr). Both $BaMn_2P_2$ and $SrMn_2P_2$ were obtained as black microcrystalline products. Small crystals of $BaMn_2P_2$ were obtained from heating once at 1100°C for 20 hr. The crystals formed as small black plates on the surface of the pellet. This synthetic procedure is a modification of previously reported syntheses by Mewis (15, 16).

Frequently, small amounts of MnP or Mn_2P impurities (undetectable by X-ray powder diffraction) were present in the samples, deduced from the magnetic measurements. In order to prepare materials free of these magnetic impurities, a 5–10% excess of the alkaline earth metal was successfully used.

Characterization

The products were examined in a dry box under an atmosphere of N_2, then ground with a mortar and pestle, mixed with silicon, and placed between two pieces of cellophane tape so they could be characterized via X-ray diffraction. Powder patterns were obtained with an Enraf–Nonius Guinier camera utilizing $CuK\alpha_1$ radiation (λ = 1.5405981 Å). These were then compared to patterns calculated from crystal structure data using the program POWDER (17). Diffraction line positions were read and 2θ values, d-spacing, and error bars were obtained from reading these positions into the program GUIN (18). The program LATT (19) was then used to take the indexed output from GUIN and solve for the lattice parameters. The lattice parameters obtained were a = 4.0376(6) Å, c = 13.063(3) Å (Ba) and a = 4.1680(5) Å, c = 7.137(1) Å (Sr). These are in good agreement with the literature values of a = 4.037(1) Å, c = 13.061(1) Å (Ba) (16) and a = 4.168(1) Å, c = 7.132(1) Å (Sr) (15).

A crystal of $BaMn_2P_2$ was mounted on a fiber, transferred to a Syntex R3m/v diffractometer, and placed under a cold stream of nitrogen. The cell parameters and space group indicated that the crystal was $BaMn_2P_2$.

Magnetic Susceptibility Measurements

A Quantum Design SQUID magnetometer with the high temperature oven option was employed for making magnetic measurements. All samples were cooled in zero field. Magnetization vs field data were taken at 10 K from 100 to 10,000 G, and magnetism vs temperature data were obtained in a field of 5000 G from 10 to 300 K. High temperature data were obtained from 300 to 750 K in a field of 10,000 G.

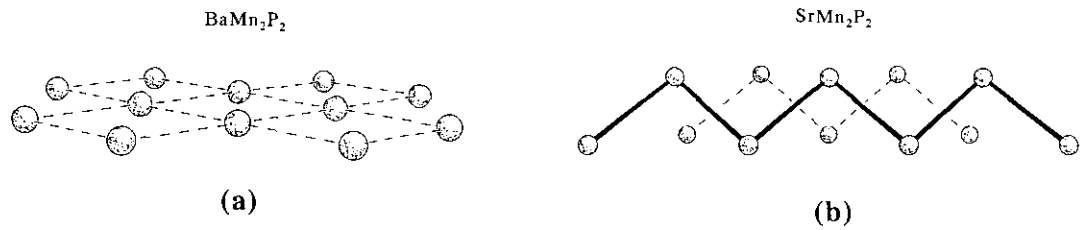

FIG. 2. Manganese networks in (a) $BaMn_2P_2$ (square net) and (b) $SrMn_2P_2$ (corrugated net).

Neutron Diffraction Measurements

Neutron diffraction data were obtained at the McMaster nuclear reactor using neutrons of $\lambda = 1.3920$ Å obtained from a (200) copper crystal monochromator. Samples were contained in an aluminum sample cell sealed with an indium gasket under a helium atmosphere. The detector, a linear position sensitive detector, has been described previously (20, 21). A CTICRYOGENICS Model 22 closed-cycle refrigerator was used to vary the sample temperature which was monitored by a calibrated thermometer.

Data were analyzed using the DBWS 9006PC and RIETAN software packages (22, 23).

Resistivity Measurements

Temperature-dependent resistivity measurements were obtained using the standard four probe method. A Keithley Model 224 current source and a Keithley Model 196 microvoltmeter or 181 nanovoltmeter were used to measure resistivity from 15 to 300 K using the program DCRES (24). Thermal voltages were minimized by reversal of current bias. Resistivity was obtained on sintered pellets using either pressed indium or silver epoxy contacts.

Spectroscopic Studies

Spectroscopic studies were performed over the range 200–25,000 nm (6.2–0.05 eV). Optical and UV spectroscopy were performed on a Hitachi U2000 spectrophotometer. The samples were ground into mulls with mineral oil and placed between optical plates. Measurements in the near-IR were performed using a Cary 1756 spectrophotometer and in the IR using a Mattson Galaxy Series 3000 FTIR. For near-IR and IR measurements the mulls were placed between CsI plates.

RESULTS

The synthetic procedure outlined by Mewis for obtaining crystals of AMn_2P_2 (A = Sr, Ba) involves heating once to 900°C, then twice to 1100°C, and once more at 1200°C, grinding between annealings. We were unable to obtain crystals via this route; however, small crystals of $BaMn_2P_2$ were obtained by heating once at 1100°C. The crystals formed as small black plates on the surface of the pellet and they were positively identified as $BaMn_2P_2$ by single crystal X-ray diffraction. The crystals were not large enough for resistivity measurements. Mewis reported that the materials are not air sensitive; accordingly, we observed no decomposition in air over a period of weeks.

When the reaction was performed on stoichiometry, frequently MnP or Mn_2P were detected via magnetic studies. MnP is characterized by a ferromagnetic transition at 292 K and a metamagnetic transition at 50 K (25). Mn_2P is antiferromagnetic with a Néel temperature of 110 K (26). These impurities appeared to be the result of insufficient reaction and usually could be removed by subsequent annealing steps. A 5–10% excess of alkaline earth metal used in the synthesis assured the formation of magnetically pure samples.

Figure 2 shows the Mn network and Fig. 3 shows the local Mn environment for the two compounds. $BaMn_2P_2$ crystallizes in the $ThCr_2Si_2$ structure type (tetragonal, $I4/mmm$). The manganese network is square planar, each manganese coordinated to four others at 90°, and the phosphorus atoms cap the planes alternatively above and below creating tetrahedral coordination of the manganese atoms. $SrMn_2P_2$ crystallizes in the $CaAl_2Si_2$ structure type (trigonal, $P\bar{3}m1$). The structure consists of a corrugated Mn network in which each Mn atom is coordinated to three others at 90° like the corner of a cube. The local geometry is approximately tetrahedral, similar to the $ThCr_2Si_2$ structure type. In both cases, the tetrahedrons are edge shared to form $Mn_2P_2^{-2}$ sheets which are separated by the cations. The Ba cations sit in a cubic hole created by phosphorus atoms in $BaMn_2P_2$, whereas in $SrMn_2P_2$ the geometry about Sr is octahedral.

Magnetization vs field studies show that for both $BaMn_2P_2$ and $SrMn_2P_2$ the susceptibility is field independent indicating that there are no ferromagnetic or ferrimagnetic contributions to the magnetism. Magnetic susceptibility measurements as a function of temperature are presented in Fig. 4. For $BaMn_2P_2$, the susceptibility increases steadily throughout the entire temperature

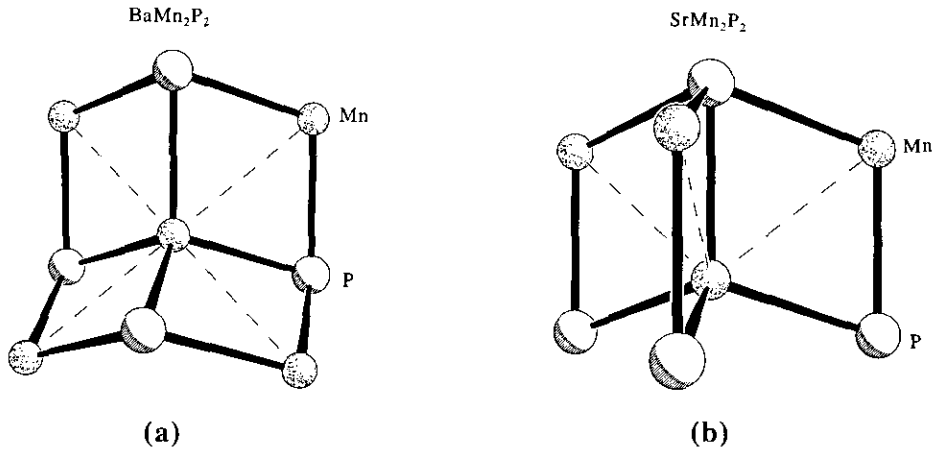

FIG. 3. The local manganese environment for (a) $BaMn_2P_2$ and (b) $SrMn_2P_2$. In both cases, the geometry of phosphorus about manganese is approximately tetrahedral.

range measured (10–750 K). This suggests that the transition temperature is very high and therefore that the coupling in the magnetic lattice is quite strong. The behavior of $SrMn_2P_2$ is more complicated. The susceptibility rises sharply in the region 10–250 K, then decreases very slightly over the range 250–750 K. The shape and breadth of the transition is indicative of a low-dimensional antiferromagnetic system (27). Measurements of the magnetic contribution to the heat capacity, dXT/dT (28) (Fig. 5) also indicate the presence of low-dimensional coupling in $SrMn_2P_2$. Note the sharp peak at 52(2) K and the gradual decrease to higher temperatures. This suggests a phase transition to a long-range ordered state below this temperature preceded by short-range order at higher temperatures. The neutron diffraction results described in the following paragraphs are consistent with this interpretation.

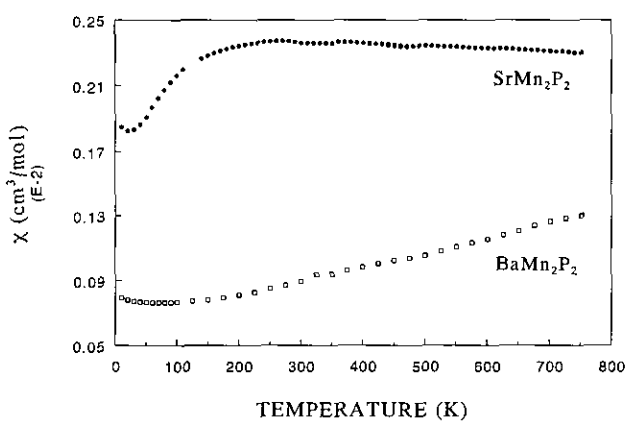

FIG. 4. Magnetic susceptibility as a function of temperature for $BaMn_2P_2$ and $SrMn_2P_2$.

The neutron diffraction pattern for $BaMn_2P_2$ at 293 K is shown in Fig. 6 which includes a fit of the diffraction profile to the published crystal structure parameters (16). Clearly, the very intense reflection at 20.72° and a weaker one at 45.76° cannot be modeled by the crystal structure alone. These diffraction peaks can be indexed as (011) and (121), respectively, on the chemical cell. In view of the magnetic susceptibility data shown in Fig. 4, it is reasonable to assign these as magnetic reflections arising from a long-range ordered antiferromagnetic state. This can be verified by a detailed analysis of the diffraction pattern.

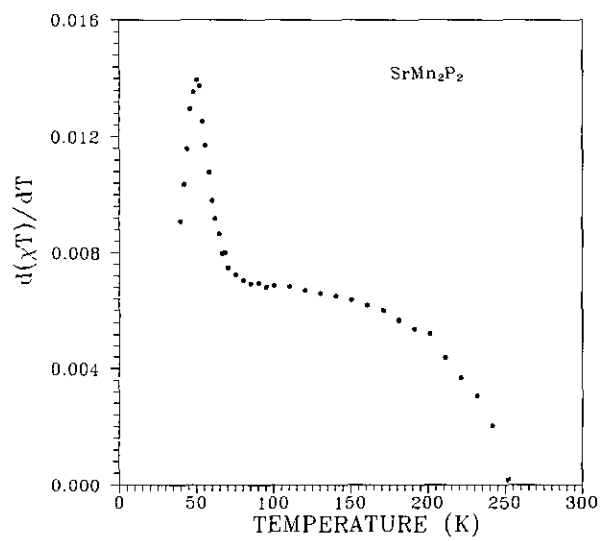

FIG. 5. An estimate of the magnetic contribution, dXT/dT, to the $SrMn_2P_2$ heat capacity (28). Susceptibility data for this analysis were obtained at a field of 2000 g at intervals of $\Delta T = 2$ K for the range 45 K $\leq T \leq$ 65 K and at $\Delta T = 5$ K for the remaining temperatures. Data below 40 K were not included due to the presence of a Curie–Weiss tail.

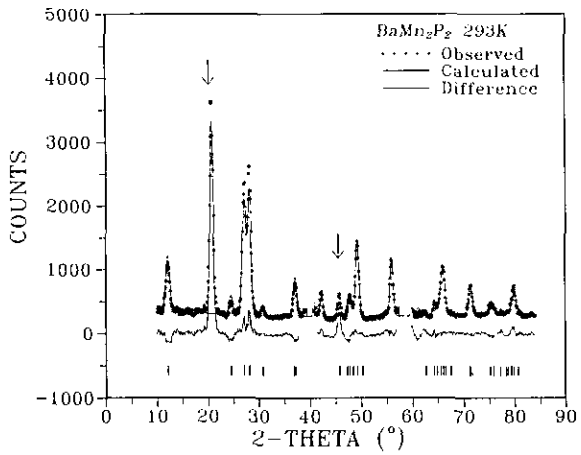

FIG. 6. Powder neutron diffraction pattern of $BaMn_2P_2$ at 293 K. The crosses are data points and the solid line is the calculated profile based only on the chemical cell. A difference profile is also shown. The vertical lines locate Bragg peak positions and the arrows identify probable magnetic reflections. Peaks from the aluminum sample cell have been removed.

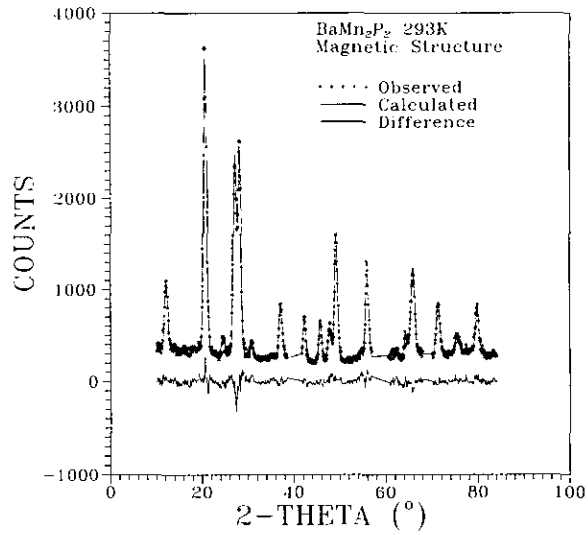

FIG. 7. Fit of the powder neutron diffraction profile for $BaMn_2P_2$ at 293 K to a combined chemical and magnetic structure. The refined parameters are given in Table 1.

The magnetic reflections can be indexed on the chemical cell indicating that the magnetic and chemical cells are identical in dimension, i.e., the propagation vector $\mathbf{k}$ = (000). There are four Mn atoms per cell at (0 $\frac{1}{2}$ $\frac{1}{4}$) and ($\frac{1}{2}$ 0 $\frac{1}{4}$) and those generated by the I-centering at ($\frac{1}{2}$ 0 $\frac{3}{4}$) and (0 $\frac{1}{2}$ $\frac{3}{4}$). A change of origin by (0 0 $\frac{1}{4}$) transforms these to (i) ($\frac{1}{2}$ 0 0), (ii) ($\frac{1}{2}$ 0 $\frac{1}{2}$), (iii) (0 $\frac{1}{2}$ $\frac{1}{2}$), and (iv) (0 $\frac{1}{2}$ 0). Thus, the magnetic sublattice is identical to that of the well-known orthorhombic perovskites (29). The four possible coupling schemes are F (+ + + +), G (+ − + −), C (+ + − −), and A (+ − − +), where the sequence of spin correlations is based on the numbering order already given. The magnetic reflections (011) and (121) belong to the grouping l = 2n + 1, $h + k$ = 2n + 1, which is consistent with a type G structure (29).

A fit to the diffraction profile for a type G model, using the program RIETAN, is shown in Fig. 7 and the results are listed in Table 1. The refined magnetic moment for Mn(II) of 4.2(1) μ_B is reasonable for the high spin state and the spins lie parallel to the c-axis. To model both the crystal and magnetic structures, it was necessary to use the reduced symmetry space group $P2$ (a-axis unique). The successful fitting of the room temperature diffraction profile confirms that $BaMn_2P_2$ is antiferromagnetically ordered. The measured Mn(II) moment is near the expected maximum of 5.0 μ_B, confirming that the T_c for this compound is well above room temperature.

The magnetic structure of $BaMn_2P_2$ is different from the magnetic structures observed in the compounds RMn$_2$X$_2$ (R = rare earth metal, X = Si, Ge) also of the $ThCr_2Si_2$ structure type (5). In these compounds, the spins within the Mn layers (ab plane) are aligned ferromagnetically. These layers can then be assembled either ferromagnetically (type F structure) or antiferromagnetically (type A structure) along c.

TABLE 1
Results of a Combined Crystal and Magnetic Structure Refinement of $BaMn_2P_2$ at 293 K

Wavelength (Å)		2θ-range (°)	Step Size (°)
1.3920		10.0–84.0	0.10
Cell parameters (Å)			
a = 4.037(1)			
c = 13.052(4)			
Space group	$I4/mmm$		
Ba in 2a	B(Å^2)	= 0.11(22)	
Mn in 4d	B(Å^2)	= 1.1(3)	
	Magnetic moment	= 4.2(1) μ_B	
	Moment direction	= 0.0° to c-axis	
P in 4e	z	= 0.3548(56)	
	B(Å^2)	= 1.00(21)	
Bragg	R_B = 0.0271		
Weighted profile	R_{WP} = 0.0818	Number profile points[a]	= 655
Profile	R_P = 0.0617	Number parameters refined[b]	= 20
Expected	R_E = 0.0442	Number independent reflections	= 44

[a] The regions containing aluminum sample can reflections were omitted.

[b] In addition to those listed in the table, a zero point, background (5 parameters), peak width (3 parameters), peak asymmetry, scale factor, and preferred orientation (2 parameters) were refined.

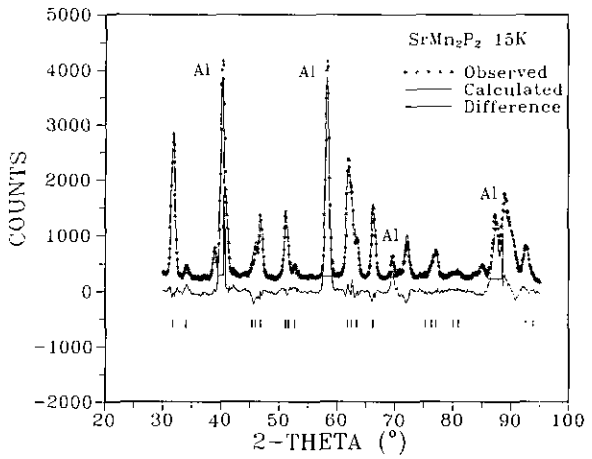

FIG. 8. Powder neutron diffraction profile for $SrMn_2P_2$ at 15 K for the 2θ range where magnetic reflections make a negligible contribution. Crosses represent the data and the solid line is the fitted profile. A difference plot is also shown. The vertical lines locate Bragg peak positions. Aluminum sample cell peaks are indicated. Refined parameters for both 15 and 293 K are shown in Table 2.

TABLE 2
Refined Structure Parameters for $SrMn_2P_2$ at 15 and 293 K

	Temperature (K)	
	293	15
Wavelength (Å)	1.3920	1.3920
2θ range (°)	10.0–94.0	31.0–94.0
Step size (°)	0.10	0.10
Cell parameters		
a (Å)	4.1629(7)	4.1562(5)
c (Å)	7.130(2)	7.096(1)
c/a	1.713	1.707
Space group	$P\bar{3}m1$	$P\bar{3}m1$
Z	1	1
Sr (B(Å^2))	0.10(15)	0.305(75)[a]
Mn (z)	0.6164(14)	0.6005(16)
Mn (B(Å^2))	0.80(23)	0.305(75)[a]
P (z)	0.2638(11)	0.2496(14)
P (B(Å^2))	0.85(15)	0.305(75)[a]
Bragg R_B	0.0879	0.0834
Weighted profile R_{WP}	0.103	0.139
Profile R_P	0.076	0.0973
Expected R_E	0.043	0.043
Number of profile points	788	592
Number parameters refined	16	14
Number independent reflections	24	20

[a] Overall temperature factor.

The case for $SrMn_2P_2$ is considerably more complex. Neutron diffraction data sets were obtained at fifteen temperatures between 15 and 293 K, inclusively. Superlattice reflections of magnetic origin, which will be described shortly, were observed below about 160 K. The crystal structure was refined at 293 and 15 K and the results are shown in Fig. 8 (15 K) and Table 2 (both temperatures). The refined unit cell and positional parameters are in reasonable agreement with previous X ray work at room temperature (15). Note the significant shrinkage in cell constants between 293 and 15 K.

Figure 9 shows data sets at 15 and 180 K and the difference plot. The dashed line locates the zero in the difference data. The magnetic contribution is negligible above 160 K, so 180-K data were chosen to minimize differences in cell constants between the two temperatures. The negative difference background is attributed to a paramagnetic contribution in the 180-K data which has shifted to the Bragg peaks of the 15-K data. This is good evidence for the magnetic origin of most of the new features in the low temperature data. There are six of these, one of which, D, is centered on the very intense (011), (101) chemical structure reflection. The intensity of D is only 10% of the (011), (101) peak and its status is unclear. Therefore, this reflection is not considered in the discussion which follows.

Of the remaining five difference peaks, which are listed in Table 3, all except B and E overlap, to some extent, reflections from the chemical cell. B and F can be indexed as $(\frac{1}{2}\ \frac{1}{2}\ 0)$ and $(0\ \frac{1}{2} \pm \frac{3}{2})$, $(\frac{1}{2}\ 0 \pm \frac{3}{2})$ on the chemical cell, respectively. That is, the magnetic cell parameters are $a_{MAG} = 2a$ and $c_{MAG} = 2c$ where a and c are the chemical cell parameters. Reflections A, C, and E cannot be indexed on this cell nor on any likely commensurate cell

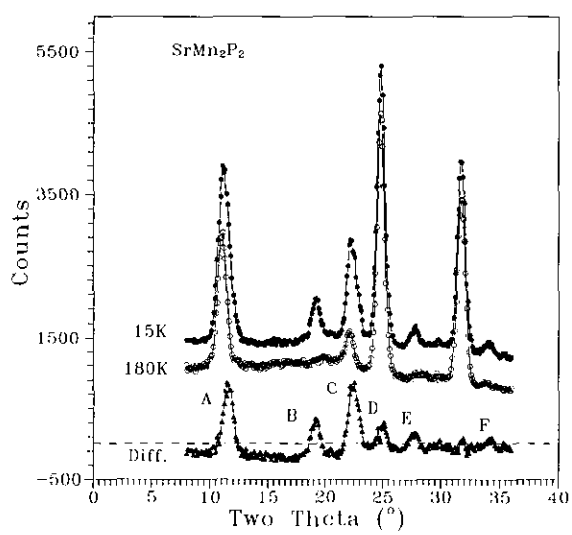

FIG. 9. Powder diffraction data for $SrMn_2P_2$ at 15 and 180 K in the 2θ range where magnetic reflections are important. The two data sets have been offset slightly for clarity. A difference plot is shown and six difference peaks, A–F, are identified. The dashed line locates the zero for the difference data.

TABLE 3
Positions of the Magnetic Superlattice Reflections at 15 K in $SrMn_2P_2$

Label	2θ (°)	d (Å)
A	11.74(1)	6.840
B	19.36(1)	4.139
C	22.56(1)	3.558
E	27.95(1)	2.882
F	34.30(1)	2.360

such as $\sqrt{3}a \times \sqrt{3}a \times c$. Thus, these three features indicate an incommensurate component to the magnetic structure. Peak C is also broader than the resolution-limited width for a single reflection which indicates contributions from more than one superlattice line.

It was possible to follow the temperature development of four of the five peaks, F was too weak to give reliable results. For B and E this was straightforward, but A and C are overlapped, as mentioned, by the (001) and (100) chemical cell reflections. For these latter cases the intensities at each temperature were determined by fitting the total envelope to a single Gaussian and then subtracting the intensity at 293 K. The results are shown in Fig. 10. Clearly, the temperature dependence of B is distinct from that of A and C. In the former case there is a rapid decline near 52 K with zero intensity above 60 K. This behavior is consistent with a phase transition to a long-range ordered state.

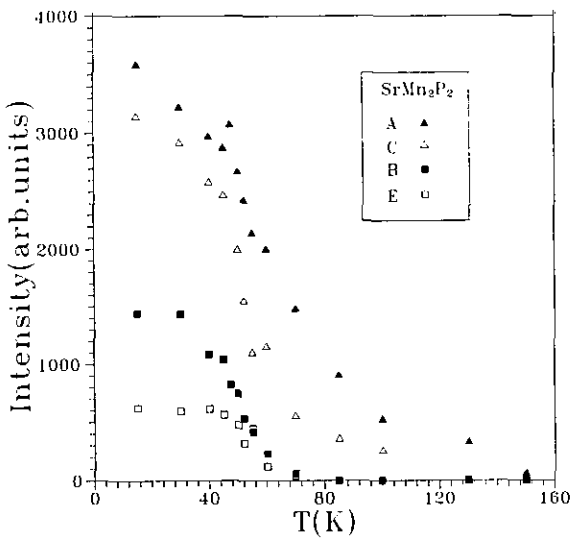

FIG. 10. Temperature dependence of the intensity of the magnetic reflections A (11.7°), B (19.4°), C (22.6°), and E (27.9°) of $SrMn_2P_2$. The height of the symbols approximates the statistical error in the intensities.

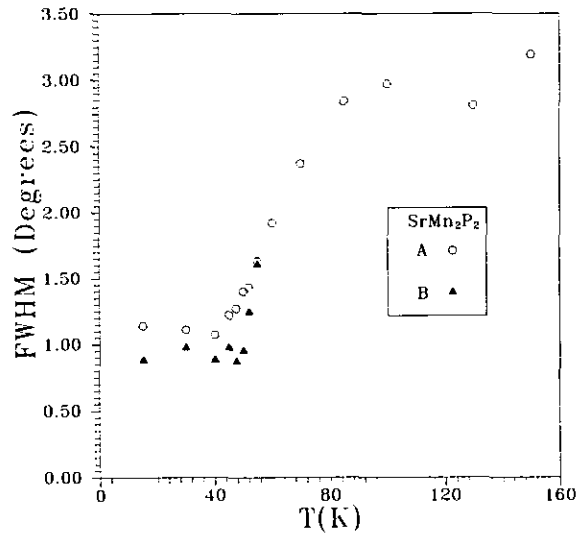

FIG. 11. Temperature dependence of the line width, FWHM, in degrees for peaks A (11.7°) and B (19.4°) of $SrMn_2P_2$. The height of the symbols approximates the statistical error in the line widths.

Reflections A and C also show a pronounced drop near 52 K but intensity persists out to nearly 160 K which is roughly three times the ordering temperature, T_c. Also, data below T_c show no indication of an approach to saturation, unlike the behavior of reflection B. The behavior of peak E above T_c is difficult to assess due to the relatively weak intensity.

The behavior of reflections A and C is indicative of short-range order which can persist well above T_c. If this is the case then the peak widths of these reflections should increase markedly above the apparent T_c. A detailed analysis was carried out for reflection A which is overlapped by the (001) chemical cell reflection. The diffraction profile in this range was analyzed as two Gaussians. The position, width, and intensity of the (001) reflection was determined from a data set at 160 K, which had no observable contribution from the super cell reflection, and was held constant during the analysis of lower temperature data. The remainder of the profile was fit to a second Gaussian with variable position, width, and intensity. Strictly speaking, one would not anticipate a Gaussian lineshape above T_c, but given the resolution of the experimental data, a more sophisticated analysis was deemed unwarranted. The results of this analysis are shown in Fig. 11 compared with a straightforward fit to the single peak at 19.4°, B.

The linewidth for B is constant up to 52 K and then increases sharply due, presumably, to critical scattering near T_c. For reflection A the line width is also constant below T_c but increases to values of three times the low temperature width by 85 K which is the expected behavior for a system with short-range magnetic correlations well above T_c.

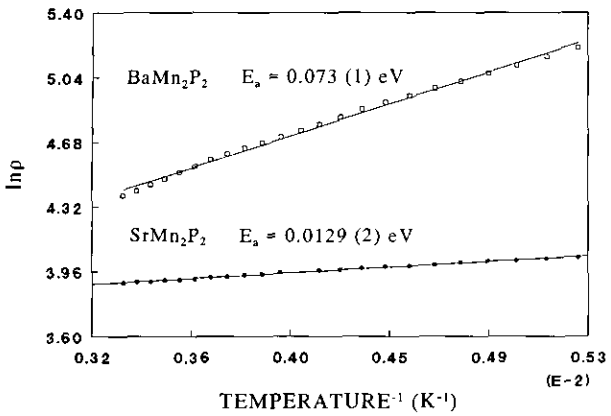

FIG. 12. Plot of ln ρ vs $1/T$ data for $BaMn_2P_2$ and $SrMn_2P_2$ for the region 200–300 K.

It is clear from the above that the magnetic structure of $SrMn_2P_2$ is quite complex with at least two types of superlattice reflections, one set, B and F belonging, apparently, to a commensurate supercell $2a \times 2a \times 2c$ and arising from long-range order with $T_c = 53(1)$ K. The other set is incommensurate and is associated with both long-range and short-range magnetic order. Although a detailed model for $SrMn_2P_2$ is yet lacking, it is clear that Mn(II) is high spin rather than low spin.

The temperature-dependent resistivity of both the Sr and Ba analogs indicates semiconducting behavior. A plot of ln ρ vs $1/T$ is linear over the temperature range 200–300 K for both samples as illustrated in Fig. 12. The activation energies are calculated to be very small, 0.073(1) eV for $BaMn_2P_2$ and 0.0129(2) eV for $SrMn_2P_2$, suggesting these are small bandgap semiconductors. In accordance, no optical bandgap was observed from spectroscopic studies in the energy region 6.2–0.05 eV.

DISCUSSION

The $CaAl_2Si_2$ structure type is observed only for d-counts of d^0, d^5, and d^{10}; whereas the $ThCr_2Si_2$ structure type is known for all d electronic configurations (30). Zheng and Hoffmann have performed theoretical calculations in order to understand why the $CaAl_2Si_2$ structure type is stabilized for d^0, d^5, and d^{10} metals (14).

The Zheng–Hoffmann approach is based on extended Hückel band theory and takes into account bonding only within the $Mn_2P_2^{-2}$ network. Correlation effects are thus ignored, as is any contribution from the counter cation to the lattice energy stabilization. It is noted that the calculations are for "low spin" configurations for Mn which is, presumably, another way of indicating that correlation is neglected. The calculations show that the $CaAl_2Si_2$ type is favored over the $ThCr_2Si_2$ type for d^0 and d^{10} configurations, which is generally consistent with observation. For d^5 the situation is more ambiguous and, in fact, the $ThCr_2Si_2$ type is favored, though only by a small energy. Zheng and Hoffmann comment that this situation could be reversed in the case of "high spin" d^5 for the $CaAl_2Si_2$ type, but a detailed calculation is not presented and is indeed beyond the scope of their method.

In the present case $SrMn_2P_2$ exhibits the $CaAl_2Si_2$ type and $BaMn_2P_2$ the $ThCr_2Si_2$ type. A strightforward application of the Zheng–Hoffmann analysis would require that $SrMn_2P_2$ be high spin and $BaMn_2P_2$ be low spin. Our experiments show that both compounds are high spin antiferromagnets, a result established unambiguously by neutron diffraction, and semiconducting. It is thus clear that the Zheng–Hoffmann analysis cannot be applied straightforwardly to these materials as $BaMn_2P_2$ does not exhibit the Pauli paramagnetic, metallic behavior which would be expected if it were a low spin material.

Evidently, for these d^5 compounds a localized electron, quasi-ionic model would be more appropriate. Detailed lattice energy calculations based on such an approach do not, to our knowledge, exist for these two compounds. It is likely, nonetheless, that the coordination preference of the counter cation makes a large contribution to the lattice energy. Indeed, the choice of structure type for the series AMn_2P_2 (A = Ca, Sr, Ba) can be rationalized on this basis. The $CaAl_2Si_2$ structure in which the counter ion is in a sixfold octahedral site, is found for the smaller Ca and Sr ions while the Ba compound crystallizes in the $ThCr_2Si_2$ structure where the cation coordination is eightfold cubic. Thus the structure type for d^5 systems may be defined by the coordination preference of the cation.

The complexity of the magnetic structure of $SrMn_2P_2$ is in sharp contrast to the simple situation for $BaMn_2P_2$. This can be understood given the different crystal structures of the two materials and especially the contrasting symmetry of the Mn(II) sublattices. As mentioned previously the Mn(II) ions form square nets in $BaMn_2P_2$ and these are separated by about 7 Å and stacked in an AA fashion. The square lattice is not subject to frustration and none is introduced by the stacking mode. In contrast, the Mn(II) lattice for $SrMn_2P_2$ consists of triangular layers stacked AB to form a bilayer and these bilayers are stacked AB · · · AB · · · AB with again about a 7 Å separation. The trigonal lattice is frustrated in two dimensions and AB stacking introduces frustration in the third dimension within the bilayer. Interbilayer exchange coupling will be weakened by the 7Å separation and frustration due to the AB · · · AB stacking.

These considerations also help to explain the large difference in T_c for long-range order in these chemically similar materials. Although one might expect similar Mn–P–Mn superexchange coupling in both materials, T_c

for the Ba compound is well above room temperature and at least ten times the T_c of 53 K found for the Sr phase. Long-range ordering is due to interplanar coupling which is frustrated in $SrMn_2P_2$ but not in $BaMn_2P_2$.

ACKNOWLEDGMENTS

We thank professor D. J. Webb (Physics) for useful discussions, Professor R. N. Shelton for use of the magnetometer and diffractometer, and P. Klavins for technical assistance. S. Brock gratefully acknowledges a University of California Graduate Opportunity Fellowship. This research is supported by NSF, Division of Materials Research, DMR-9201041, and the donors of the Petroleum Research Fund administered by the ACS. J. E. G. acknowledges McMaster University for direct support of the McMaster nuclear reactor, A. Nakua for assistance with the RIETAN program, and Guo Liu for the magnetic heat capacity data.

REFERENCES

1. W. Jeitschko, R. Glaum, and L. Boonk, *J. Solid State Chem.* **69,** 93 (1987).
2. F. Steglich, J. Aarts, C. D. Bredl, W. Lieke, D. Meschede, W. Frantz, and H. Schäfer, *Phys. Rev. Lett.* **43,** 1892 (1979).
3. F. Steglich, *J. Phys. Chem. Solids* **50,** 225 (1989).
4. W. Schlabitz, J. Baumann, B. Pollit, U. Rauchschwalbe, H. M. Mayer, U. Ahlheim, and C. D. Bredl, *Z. Phys. B Condens. Matter* **62,** 171 (1986).
5. A. Szytuła, J. Leciejewicz, *in* "Handbook on the Physics and Chemistry of Rare Earths," (K. A. Gschneidner, Jr. and L. Eyring, Eds.), Vol. 12, Chap. 83. Elsevier, Amsterdam/New York, 1989.
6. Z. Zolnierek, D. Kaczorowski, and R. Troć, *J. Less-Common Met.* **121,** 193 (1986).
7. W. Jeitschko and M. Reehuis, *J. Phys. Chem. Solids* **48,** 667 (1987).
8. E. Mörsen, B. D. Mosel, W. Müller-Warmuth, M. Reehuis, and W. Jeitschko, *J. Phys. Chem. Solids* **49,** 785 (1988).
9. P. Fischer, A. Murasik, D. Kaczorowski, and R. Troć, *Physica B* **156/157,** 829 (1989).
10. M. Reehuis and W. Jeitschko, *J. Phys. Chem. Solids* **51,** 961 (1990).
11. M. Reehuis, T. Vomhof, and W. Jeitschko, *J. Less-Common Met.* **169,** 139 (1991).
12. G. Zwiener, H. Neumann, and H.-U. Schuster, *Z. Naturforsch. B Anorg. Chem. Org. Chem.* **36,** 1195 (1981).
13. M. Pfisterer and G. Nagorsen, *Z. Naturforsch. B Anorg. Chem. Org. Chem.* **38,** 811 (1983).
14. C. Zheng and R. Hoffmann, *J. Solid State Chem.* **72,** 58 (1988).
15. A. Mewis, *Z. Naturforsch. B Anorg. Chem. Org. Chem.* **33,** 606 (1978).
16. A. Mewis, *Z. Naturforsch. B Anorg. Chem. Org. Chem.* **35,** 141 (1980).
17. C. M. Clark, D. K. Smith, and G. A. Johnson, "POWD: A FORTRAN II Program for Calculating X-ray Diffraction Patterns," Version 5, Department of Geosciences, Pennsylvania State University, University Park, PA, 1973.
18. H. Imoto, "GUIN: A FORTRAN Program to Calculate Two-Theta from Film with Si Reference Lines." Iowa State University, Ames, IA, 1979.
19. F. Takusagawa and J. D. Corbert, "LATT," Iowa State Unviersity, Ames, IA, 1981.
20. J. E. Greedan, A. H. O'Reilly, and C. V. Stager, *Phys. Rev. B Condens. Matter* **35,** 8770 (1987).
21. C. W. Tompson, D. F. R. Mildner, M. Mehregany, J. Sudol, R. Berliner, and W. B. Yelon, *J. Appl. Crystallogr.* **17,** 385 (1984).
22. A. Sakthivel and R. A. Young, "DBWS—9006PC Rietveld Analysis of X-ray and Neutron Powder Diffraction Patterns," School of Physics, Georgia Institute of Technology, Atlanta, GA, 1992.
23. F. Izumi, "Rietan–Rietveld Analysis System," National Institute for Research in Inorganic Materials, 1-1 Namiki, Tsukuba-shi, Ibaraki 305.
24. J. E. Sunstrom, IV, "DCRES: A QuickBASIC Program for Resistivity Data Collection and Statistical Analysis," University of California, Davis, CA, 1990.
25. E. E. Huber, Jr. and D. H. Ridgley, *Phys. Rev. A* **135,** 1033 (1964).
26. S. K. Malik and R. Vijayaraghavan, *Phys. Lett. A* **28,** 648 (1969).
27. R. Navarro, J. J. Smit, L. J. de Jongh, W. J. Crama, and D. J. W. Ijdo, *Physica B* **83,** 97 (1976).
28. M. E. Fisher, *Philos. Mag.* **17,** 1731 (1962).
29. E. F. Bertaut, in "Magnetism," (G. T. Rado and H. Suhl, Eds.), Vol. III, p. 149. Academic, New York, 1963.
30. P. Klüfers and A. Mewis, *Z. Naturforsch. B Anorg. Chem. Org. Chem.* **32,** 753 (1977).